Journal of the European Ceramic Society **32** (2012) p.611

# Structural and physical properties of microwave synthesized orthorhombic perovskite erbium chromite $ErCrO_3$

Jesús Prado-Gonjal [a], Rainer Schmidt [b,*], David Ávila [a], Ulises Amador [c], Emilio Morán [a]

[a] *Dpto. Química Inorgánica I, Facultad de CC. Químicas, Universidad Complutense de Madrid, 28040 Madrid, Spain*
[b] *Dpto. Física Aplicada III, Facultad de CC. Físicas, GFMC, Universidad Complutense de Madrid, 28040 Madrid, Spain*
[c] *Dpto. Química, Facultad de Farmacia, Universidad San Pablo, CEU, 28668 Boadilla del Monte, Madrid, Spain*

**Abstract**

Rare-earth chromite $ErCrO_3$ powder was synthesized from metal nitrate precursors using microwave synthesis. (Micro-) structural characterizations were performed using X-ray diffraction, Rietveld refinement High Resolution Transmission Electron Microscopy and Electron Micro-Diffraction. Magnetization vs. temperature measurements revealed anti-ferromagnetism with $T_{Neel} \approx 135$ K. An anti-ferrimagnetic moment of $\approx 0.4\ \mu_B$ was determined from magnetization vs. applied fiel measurements. Temperature dependent impedance spectroscopy (IS) indicated 3 dielectric relaxation processes: electrode interface, grain boundary and bulk. The intrinsic bulk activation energy was found to be 0.27 eV and the dielectric permittivity $\varepsilon_r$ was ≈23 in excellent agreement with Clausius–Mossotti predictions and showed no perceptible temperature dependence. This and the low $\varepsilon_r$ value suggested that $ErCrO_3$ is a dielectric rather than ferroelectric compound. IS measurements with applied dc bias revealed the signs of an unconventional type of Schottky barrier at the metallic Au electrode/ceramic $ErCrO_3$ interface.

*Keywords:* A. Microwave processing; B. Microstructure-final B. X-ray methods; C. Dielectric properties; C. Magnetic properties; Chromites

## 1. Introduction

The compound erbium chromite $ErCrO_3$ with orthorhombic perovskite structure is part of the family of rare-earth (RE) chromites $(RE)CrO_3$, which have currently attracted considerable attention due to potential application as multifunctional materials. Although these compounds have been well documented for decades, only recently magneto-electric coupling between the rare earth and the $Cr^{3+}$ cation has been claimed and the rare earth chromites were suggested to belong to a new family of multiferroics.[1,2] Since $ErCrO_3$ possesses a canted antiferromagnetic ordering with a weak ferri-magnetic moment below $T_N \approx 135$ K[3] and ferroelectricity has been suggested,[4,5] this compound has been regarded a promising candidate for multiferroic coupling to occur. The magnetic structure of this compound is rather intriguing and 3 types of antiferromagnetic exchange interactions, $Cr^{3+}$–$Cr^{3+}$, C r $^{3+}$–$Er^{3+}$ and $Er^{3+}$–$Er^{3+}$, have been reported.[3] The crystal structure of $ErCrO_3$ has been considered as an orthorhombic perovskite (S.G. Pnma with cell setting $\sqrt{2}a_p \times 2a_p \times \sqrt{2}a_p$, where $a_p$ is the basic cubic perovskite lattice parameter). In the perovskite Pnma setting the tilting of the oxygen octahedra can be indexed in the Glazier notation as $a^+b^-b^-$.[6] It is important to note that the Pnma space group is centrosymmetric, which would be inconsistent with the ferroelectricity claimed in this material. In order to resolve the equivalent contradiction in $YCrO_3$ (with the same Pnma space group), Ramesha et al.[7] proposed the concept of local non-centrosymmetry, where a local character of the Cr off-centering and a small value of the atomic displacement were claimed to be sufficien to cause weak ferroelectric polarization.

Conventionally, $ErCrO_3$ is synthesized in air by the solid-state reaction method at high temperatures ($T > 1200$ °C). The diffusion of ions using the solid-state synthesis method is rather slow though and, therefore, requires high temperatures and long heating periods with intermediate grinding in

* Corresponding author.
*E-mail address:* rainerxschmidt@googlemail.com (R. Schmidt).

order to achieve good homogeneity.[8] A variety of alterna-tive synthetic methods are being used nowadays in order to obtain ceramic materials in a more time and energy-efficien way, such as self-propagating high-temperature synthesis[9] or metathesis of metal chlorides.[10] In this paper, we present the novel route of microwave assisted synthesis of $ErCrO_3$ using a domestic microwave apparatus working at 2.45 GHz frequency (12.3 cm wavelength).[11,12] The rather low energy of 2.45 GHz microwave electromagnetic radiation (0.0016 eV) is too weak to break any chemical bonds (hydrogen bond energy ≈0.21 eV) and microwave energy absorption can occur only in certain circumstances. If the material is a conduc-tor (metal), microwaves will be reflecte and no energy is transferred. For dielectric materials microwave energy can be absorbed through the excitation of dipole moments which directly couple to the electromagnetic wave and heat will be generated.[13–16] In case that the precursor reactants are poor microwave absorbers, energy absorption can be enhanced by using microwave susceptors such as amorphous carbon, SiC or graphite.[17]

The aims of this work were: (a) to produce single-phase $ErCrO_3$ powder by a novel route of microwave irradiation of precursor nitrates, (b) to characterize the structure and micro-structure, and (c) to study magnetic and dielectric properties and the potential for multifunctional applications.

## 2. Experimental

### *2.1. Synthesis*

Metal nitrate precursors $Cr(NO_3)_3{\cdot}9H_2O$ (98%) and $Er(NO_3){\cdot}5H_2O$ (99.9% Sigma–Aldrich) were weighed and mixed with 5% (wt.) amorphous carbon acting as microwave susceptor. The mix was mechanically homogenized and compacted into pellets of 12 mm diameter, which were placed in a porcelain crucible and irradiated in a domestic microwave oven for 10 min (2.45 GHz and 800 W). Consecutively, the pellets were crushed and the amorphous powder was heated in a conventional furnace in air at (A) 500 °C for 2 h for crystallization in order to form the precursor $ErCrO_4$, and (B) at 800 °C for 2 h to form $ErCrO_3$. Phase purity was confirme by powder X-ray diffraction (XRD) and pellet compaction was performed in a 1 ton die press for 5 min followed by densificatio sintering in air at 1300 °C for 15 h.

### *2.2. Structural characterization*

Purity and structure of the samples were examined by powder XRD on a Bruker D8 high-resolution diffractometer using monochromatic $CuK_{\alpha 1}$ ($\lambda = 1.5406$ Å) radiation obtained with a germanium primary monochromator, and equipped with a solid-state rapid LynxEye detector. For structural refinemen the measured angular range, the step size and counting times were adjusted in order to ensure sufficien resolution. The structural refinement were carried out by the Rietveld method using FullProf software.[18]

Scanning Electron Microscopy (SEM) studies were carried out on powder and sintered pellets using an electron microscope JEM 6335 F with a Field Emission Gun operating at 10 kV, fitte with an X-ray Energy Dispersive Spectroscopy (XEDS) analyzer. Powder XEDS analysis was performed on 10 $ErCrO_3$ micro-crystallites (grains), where three different areas of each crystallite were investigated in order to reliably determine the average cation composition.

Samples for Transmission Electron Microscopy (TEM) were prepared from $ErCrO_3$ powder, suspended and ultrasonically dispersed in butanol and placed on a Cu grid with holey carbon film Selected Area Electron Diffraction (SAED), Electron Microdiffraction and High Resolution TEM (HRTEM) experiments were performed using a JEOL 3000F microscope with a resolution limit of 1.1 Å. SAED patterns were recorded with a parallel beam using a 70 μm C2 aperture and a 0.7 mm diffraction aperture. The microdiffraction patterns were obtained with a nearly parallel incident beam using a 50 μm C2 aperture and the incident electron beam was focused on the specimen with a spot size in the range of 2 nm. The crystallographic analysis was performed following the method proposed by Morniroli and Steeds.[18]

HRTEM images were recorded with an objective aperture of 70 μ m centered on a sample spot within the diffraction pattern area. Fast Fourier Transforms (FFT) of the HRTEM images were performed in order to reveal the periodic contents using the Dig-ital Micrograph package.[19] The experimental HRTEM images were also compared to simulated images using MacTempas software.[20] Such computations were performed using informa-tion from (A) the $ErCrO_3$ structural parameters obtained from the Rietveld refinement (B) the microscope parameters such as voltage (300 kV) and spherical aberration coefficien (0.6 mm), and (C) the specimen parameters such as zone axis and thick-ness.

### *2.3. Physical property measurements*

Magnetic susceptibility measurements were performed on $ErCrO_3$ powders using a Quantum Design XL-SQUID magnetometer in the temperature range of 2–300 K at 1 kOe applied magnetic field The temperature dependence of the magnetization was measured following Zero Field Cooled and Field Cooled (ZFC-FC) procedures. The ferri-magnetic hysteresis cycles were recorded at 25 K from magnetization vs. applied magnetic fiel measurements.

Impedance spectroscopy (IS) measurements on sintered pellets with dc sputtered Au electrodes were carried out at 150–550 K using a Novocontrol Alpha-A High Performance Frequency Analyzer equipped with a liquid nitrogen cooled sample chamber. A 100 mV amplitude alternating voltage signal was employed and IS data was obtained at each temperature in terms of the real and imaginary parts of the impedance ($Z'$–$Z''$) at various frequencies ($f$) between 0.5 Hz and 3 MHz. Furthermore, IS measurements were carried out at 200 K with applied dc bias of 0 V, 0.32 V and 1 V and a superimposed ac amplitude of 100 mV.

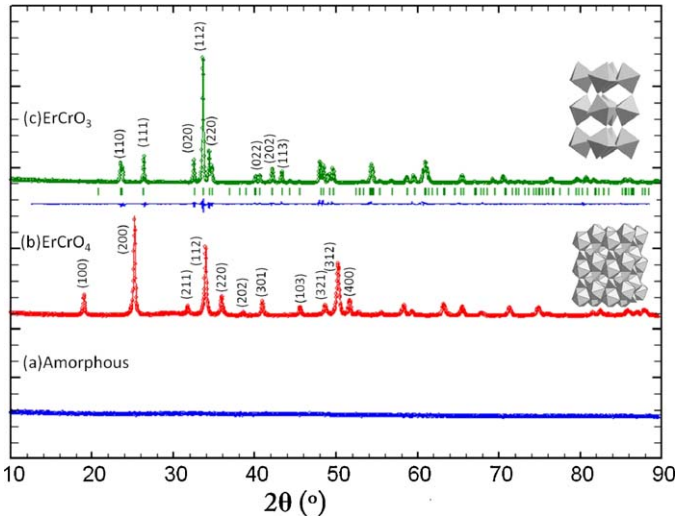


Fig. 1. X-ray diffraction patterns of (a) amorphous powder obtained after microwave irradiation, (b) $ErCrO_4$ with zircon-type structure, and (c) orthorhombic perovskite $ErCrO_3$ with Rietveld fit showing experimental data (circles), calculated pattern (continuous line) and their difference (continuous blue line underneath). The positions of the Bragg reflection are indicated by vertical bars.

Table 1
Refined structural parameters for $ErCrO_3$ obtained from XRD data.

| | |
|---|---|
| *a* (Å) | 5.21389 (4) |
| *b* (Å) | 7.50391 (6) |
| *c* (Å) | 5.50302 (4) |
| *Er position 4c* | |
| *x* | 0.0680 (1) |
| *z* | −0.0180 (1) |
| *U**100 (Å$^2$) | 0.031 (2) |
| *Cr position 4b* | |
| *U**100 (Å$^2$) | 0.23 (1) |
| *O(1) position 4c* | |
| *x* | 0.4646 (7) |
| *z* | 0.1081 (7) |
| Occ | 1.00 (1) |
| *U**100 (Å$^2$) | 0.13 (5) |
| *O(2) position 8d* | |
| *x* | 0.3022 (4) |
| *y* | 0.0521 (4) |
| *z* | −0.3059 (6) |
| Occ | 1.00 (1) |
| *U**100 (Å$^2$) | 0.13 (5) |

S.G. Pnma: 4*c* (*x* 1/4 *z*), 4*b* (0 0 1/2), 8*d* (*x y z*). $\chi^2 = 3.70$, $R_{wp} = 3.43\%$, $R_{exp} = 1.74\%$, $R_B = 2.33\%$.

## 3. Result and discussion

### *3.1. Reaction mechanism and (micro-) structural characterization*

The reaction mechanism for the $ErCrO_3$ formation from nitrate precursors can be described by a three-step process:

(i) Formation of an amorphous material after 10 min microwave irradiation.
(ii) Formation of polycrystalline $ErCrO_4$ at 500 °C (2 h) with zircon-type structure and tetragonal symmetry, S.G. $I4_1/amd$ (# 141).[21]
(iii) Formation of $ErCrO_3$ at 800 °C (2 h) with a distorted perovskite structure and orthorhombic symmetry, S.G. Pnma (# 62).

Fig. 1a–c shows the X-ray powder diffraction patterns of the amorphous, the precursor zircon-type and the orthorhom-bic perovskite phases respectively. The nominal compound $ErCrO_3$ obtained at high temperature was confirme to show the expected Pnma orthorhombic perovskite structure.[22,23] In Fig. 1c the Rietveld fi curve, the XRD data and underneath the difference between model and data are shown. The fitte parameters are summarized in Table 1.

Fig. 2 shows the SEM micrographs of $ErCrO_3$ powder (Fig. 2a) and an $ErCrO_3$ sintered pellet (Fig. 2b). In powder form the $ErCrO_3$ particles form a brain-shaped structure and exhibit intra-granular fractures. These fractures were healed out during sintering, and the sintered pellet displays no significan porosity. XEDS analysis yielded an average ratio Er:Cr of 1:1.02, which corresponds to the nominal stoichiometry within experimental error.

Selected Area Electron Diffraction (SAED) patterns (not shown here) of several crystals confirme good homogeneity of the sample and the orthorhombic perovskite structure ($a$ = 5.2 $b$ = 7.5 and $c$ = 5.5 Å). Fig. 3 shows the microdiffraction patterns, which revealed the presence of glide planes and screw axes of the specimen in our particular sample. The ideal symmetry of the Zero Order Laue Zone (ZOLZ) for the [0 1 0] and [1 1 0] zone axes patterns are 2mm indicating that the crystal system must present orthorhombic symmetry, in agreement with the Pnma space group. In addition, when looking carefully at the rows of the $k$ 0 0 and 0 0 $l$ reflection in the [0 1 0] zone axis (Fig. 3a), it can be seen that dark Gjønnes–Moodie lines are crossing the reflection with $k = 2n + 1$ and $l = 2n + 1$.[22] These lines are cine-matically forbidden due to the presence of $2_1$ screw axes parallel to $a$ and $c$, but appear due to multiple diffraction.

Microstructure observations by HRTEM were performed along the zone axis [0 1 0], previously analyzed by microdiffraction. An HRTEM image with a well ordered crystal structure is shown in Fig. 4a, as it is supported by the absence of extra reflections or streaking in the FFTs displayed in the upper left side of the image. In such HRTEM image taken near the Scherzer defocus [23] of the microscope (−350 Å), the dark dots correspond to cation columns. In the image we can directly measure the $a$ and $c$ cell parameters, which correspond to 5.2 and 5.5 Å consistent with those measured by XRD. A small section of the experimen-tal HRTEM image in Fig. 4a is replaced by the simulated image as outlined by the dotted yellow rectangle. Excellent agreement between theoretical and experimental images was obtained by using a defocus value of $\Delta f = -300$ Å and a thickness $t$ = 5 0 Å in the theoretical model. Below the calculated image a sketch of the structure with the octahedra $CrO_6$ coloured in green and the $Er^{3+}$ cations in pink match perfectly with the dark dots. A view along the $b$-axis perpendicular into the crystal corresponds to a view into the image plane of Fig. 4a, where two $Er^{3+}$ cations

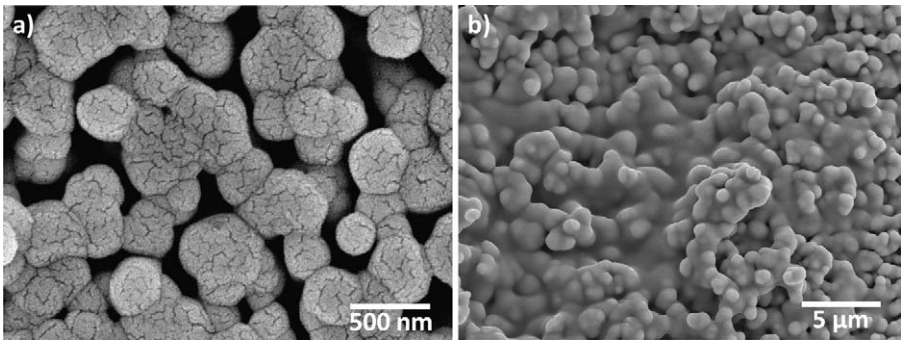


Fig. 2. Scanning electron micrograph of (a) $ErCrO_3$ powder as prepared, and (b) $ErCrO_3$ pellet after densificatio sintering at 1300 °C for 15 h.

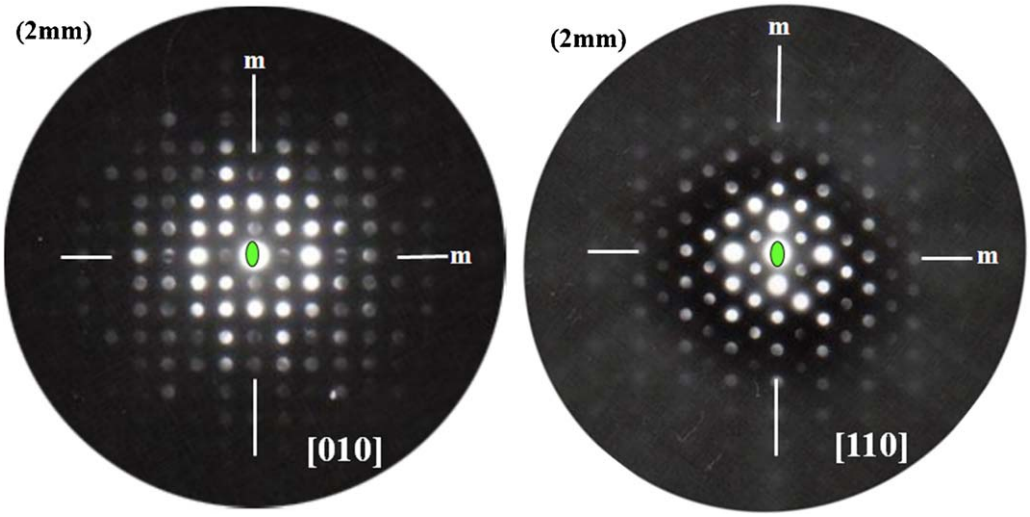


Fig. 3. Microdiffraction patterns of orthorhombic $ErCrO_3$ along [0 1 0] and [1 1 0] showing (2 mm) ideal symmetry. The characteristic Gjønnes–Moodie lines crossing the odd $k$ 0 0 and 0 0 l reflection in the [0 1 0] zone axis indicate forbidden reflection appearing due to multiple diffraction.

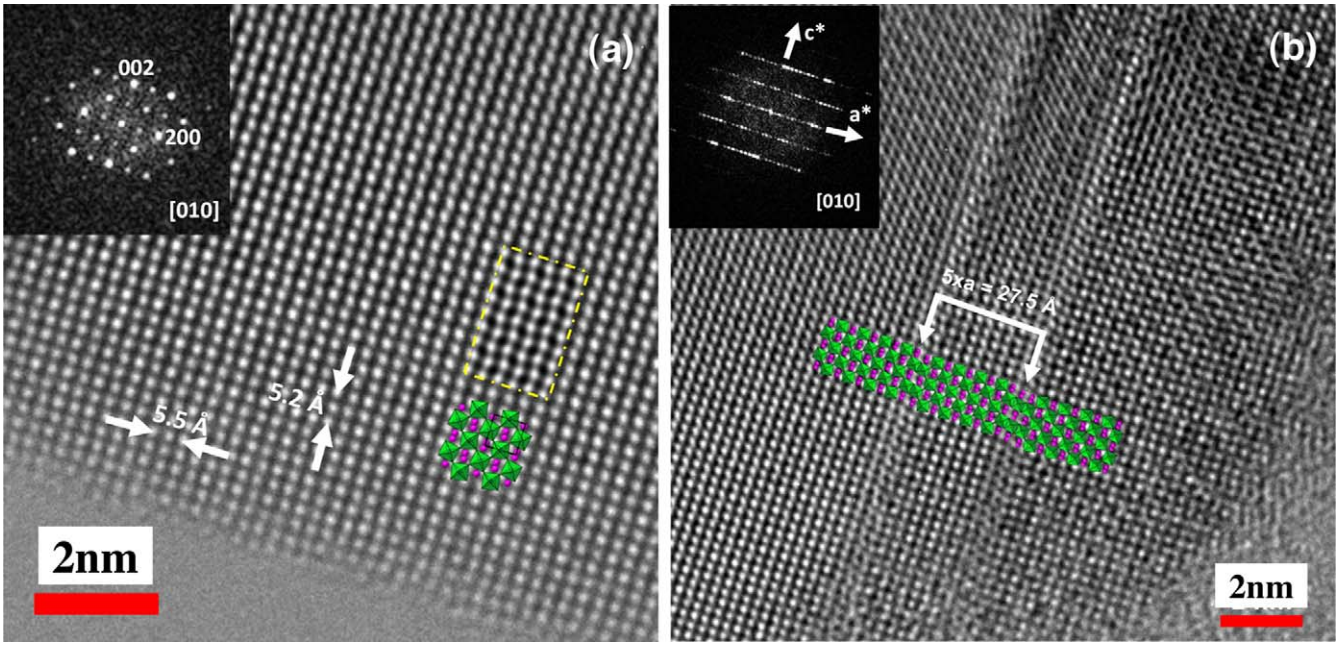


Fig. 4. (a) Experimental HRTEM micrograph along the [0 1 0] zone axis. No streaking or extra spots are evident (see the FFT images in the f gure inset). A good match between experimental and simulated images is demonstrated (dotted yellow rectangular box). (b) Dislocation defect of ~28 °A ( 5 × $a$) width. The FFT in the inset shows extra spots observed along $a$* confirmin this defect.

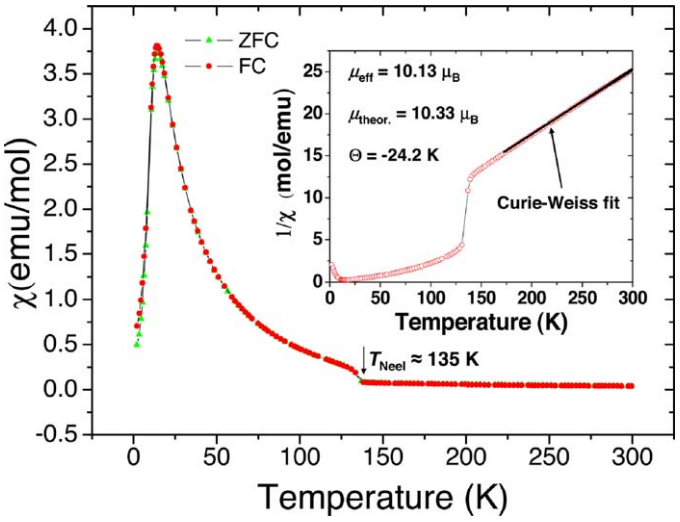


Fig. 5. Temperature dependence of the magnetic susceptibilities $\chi$ of $ErCrO_3$ at 1 kOe. ZFC and FC curves are indicated by green triangles and red circles respectively. *Inset*: Inverse susceptibility $1/\chi$. The black solid line represents the fi of the data to the Curie–Weiss law, yielding an effective magnetization $\mu_{eff} = 10.13\ \mu_B$ and a Weiss constant $\Theta = -22.1$ K.

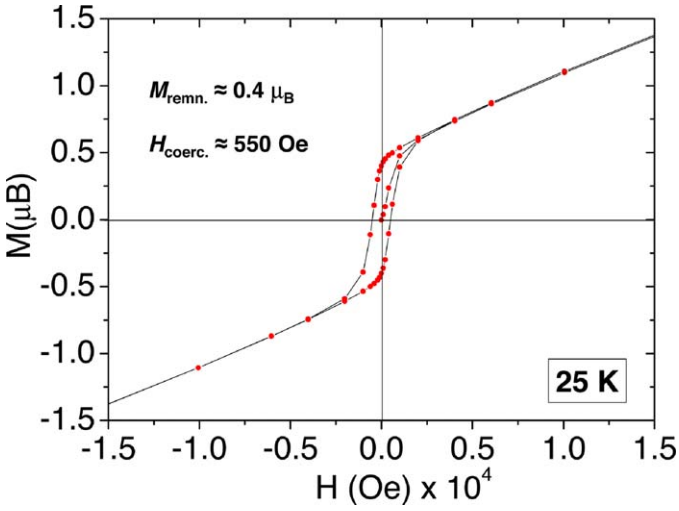


Fig. 6. Magnetization vs. applied magnetic fiel hysteresis loop at 25 K indicating remnant magnetization $M_{remn.} \approx 0.4\ \mu_B$ and a coercive fiel $H_{coerc.} \approx$ 550 Oe.

are visible in close distance in the crystal structure sketch. This is because two $Er^{3+}$ cations in two consecutive crystal cells do not align along the *b*-axis, which is a result of the orthorhombic crystal symmetry. Although HRTEM showed generally a well ordered structure in most of the crystals, in few cases it revealed the presence of local dislocation defects (Fig. 4b) responsible for the extra diffuse spots along *a** observed in the Fast Fourier Transform (FFT) pattern (inset Fig. 4b). The local dislocation here appears as a distinct area of a locally dislocated lattice of the width of fi e unit cells (see white arrows) and the shift is about 1/2 along *c* stabilized by sharing edges of the consecutive octahedra (see schematic sketch inserted into the experimental image).

### 3.2. Magnetic properties

Fig. 5 shows the temperature dependence of the molar magnetic susceptibility $\chi$ for $ErCrO_3$ measured under ZFC and FC conditions using a 1 kOe applied magnetic field The antiferromagnetic transition occurs at $T_N \approx 135$ K although a weak ferri-magnetic moment remains. Such moment arises from the canting of antiferromagnetic $Cr^{3+}$ moments as described in the literature.[3,24,25] Fig. 5 displays a $\chi$ peak around 14 K and the peak values under FC and ZFC conditions are 3.8 emu/mol and 3.7 emu/mol respectively. This peak has been observed previously by Parkin and Komarov[10] and was interpreted as a spin reorientation resulting from the anisotropic parts of the magnetic interaction between $Cr^{3+}$ and $Er^{3+}$. The inset in Fig. 5 shows the temperature dependence of the inverse susceptibility $1/\chi$. Above $T_N$, the $1/\chi$ vs. $T$ curve in the paramagnetic state follows the Curie–Weiss law: $\chi = C/(T - \Theta)$, where $C$ is the Curie constant related to the effective magnetic moment $\mu_{eff}$, $T$ is temperature, and $\Theta$ is the Weiss constant, which is usually regarded a good estimate for the Curie transition temperature. The Curie–Weiss fit indicated by the solid line in the inset of Fig. 5, yielded $C = 12.8$, $\Theta = -24.2$ K, and $\mu_{eff}$ was calculated to be 10.13 $\mu_B$ in good agreement with the theoretical value $\mu_{theor.} = 10.33\ \mu_B$ calculated from 9.58 $\mu_B$ for $Er^{3+}$ and 3.87 $\mu_B$ for $Cr^{3+}$. A negative $\Theta$ value suggests the predominance of antiferromagnetic interactions.

Hysteresis loop measurements of magnetization [$\mu_B$] vs. applied fiel [Oe] at 25 K are shown in Fig. 6 confirmin the canted antiferromagnetic structure and the presence of a ferri-magnetic moment. The remnant magnetization $M_{remn.}$ and the coercive fiel $H_{coerc.}$ are approximately 0.4 $\mu_B$ and 550 Oe respectively, indicative of a weak ferri-magnetic component.

### 3.3. Dielectric properties

Impedance spectroscopy (IS) data in terms of real ($Z'$) and imaginary ($Z''$) parts of the impedance are plotted as $-Z''$ vs. $Z'$ in Fig. 7. At 200 K 3 distinct semi-circles are displayed, which can be associated with 3 dielectric relaxation processes.[26,27] The relaxations were assigned to one intrinsic bulk and two extrinsic contributions, grain boundary (GB) and electrode–sample inter-face. An equivalent circuit model was used (shown in Fig. 7 inset) in order to fi the data at various temperatures. Conven-tionally, an ideal relaxation process can be modeled with an ideal RC element of parallel resistance and capacitance, and for interface, GB and bulk relaxations 3 RC elements can be sim-ply added in series. We have encountered non-ideal dielectric response though, which was manifested by slightly suppressed semicircles. This can be accounted for by replacing the ideal capacitor with a constant phase element (CPE).[28] In our case, an almost ideal fi was obtained using 3 R-CPE elements in series (Fig. 7).

The inset of Fig. 7 shows plots of $-Z''$ vs. $f$ and the modulus function $M''$ vs. $f$, where 3 dielectric relaxation peaks are visible in each plot. For ideal dielectric relaxations as represented by ideal RC elements the height of the peaks in $-Z''$ vs. $f$ are proportional to the resistance $R$: $-Z''(f_{max}) = R/2$ of the respective relaxation, and the height of the peaks in $M''$ vs. $f$ are inverse proportional to the capacitance $C$: $M''(f_{max}) = C_0/2C$,

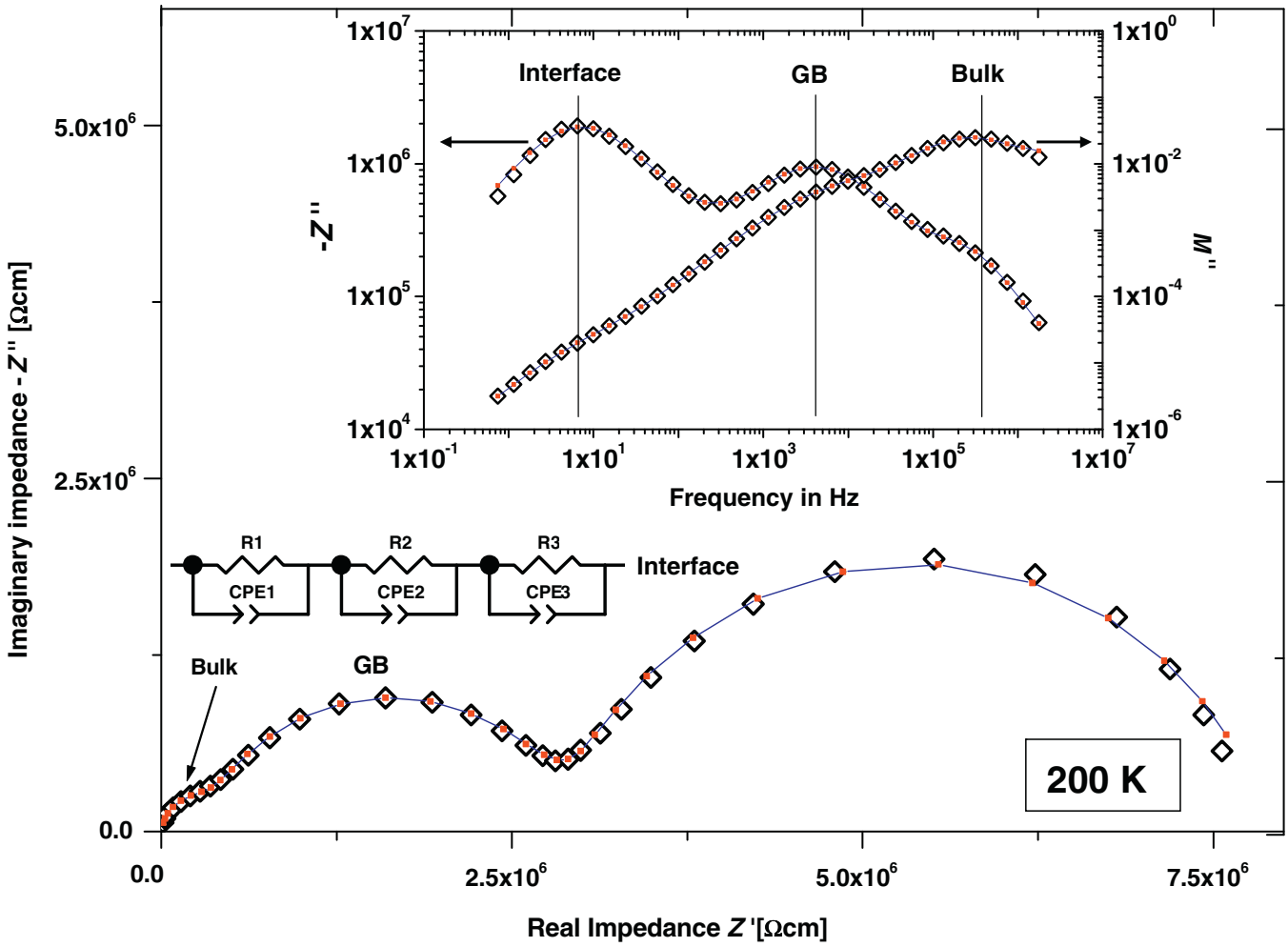


Fig. 7. Impedance spectroscopy data plotted as complex plane impedance plots of negative imaginary part of the impedance $-Z''$ vs. real part of the impedance $Z'$ at 200 K. Open symbols (◊) represent the data, solid squares (■) and solid lines represent fit using the equivalent circuit model shown within the figure *Inset*: $-Z''$ and imaginary part of the modulus function $M''$ vs. $f$.

where $C_0$ is a constant factor. Although non-ideal relaxation peaks may be slightly suppressed, the graphs in Fig. 7 inset still suggest unequivocally that the interface relaxation exhibits high resistance and high capacitance, the GB relaxation intermediate resistance and capacitance, and the intrinsic bulk relaxation small resistance and capacitance.

By using the equivalent circuit model at various temperatures we obtained the temperature dependence of the bulk resistance (R1) and capacitance (CPE1), the GB resistance (R2) and capacitance (CPE2), and the interface resistance (R3) and capacitance (C3). The CPE capacitance values obtained from the fit were corrected to conventional capacitance given in [F/cm].[29] Such values were then plotted as relative dielectric permittivity $\varepsilon_r$ vs. $T$ in Fig. 8. The intrinsic bulk $\varepsilon_r$ is in the range of 23, which is in remarkable agreement with the value of 22.7 predicted from the Clausius–Mossotti equation for dielectric materials based on the unit cell volume and the sum of the ionic polarisabil-ity of each individual atom, both at room temperature.[30] The GB permittivity is in the range of 200 and the interface capacitance in the range of 50 000. All 3 relaxations show capacitance

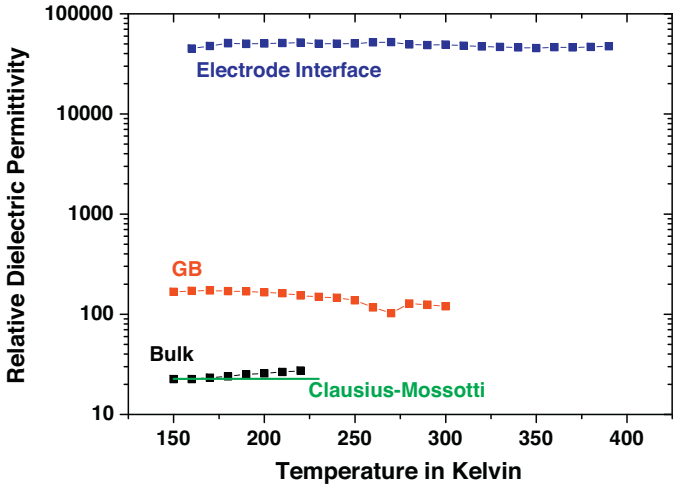


Fig. 8. Relative dielectric permittivity $\varepsilon_r$ for interface, GB and bulk relaxation processes vs. temperature $T$. The green line represents the room temperature Clausius–Mossotti prediction for dielectric $ErCrO_3$.

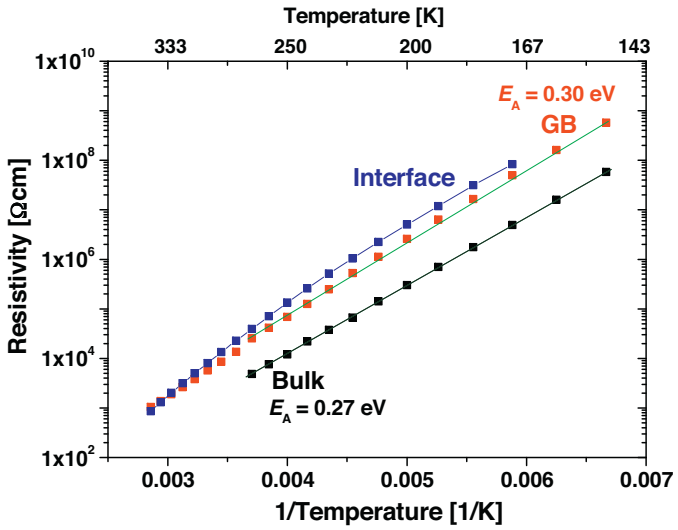


Fig. 9. Arrhenius plots of the resistivity $\rho$ for interface, GB and bulk relaxations vs. reciprocal temperature $1/T$. For the GB and bulk relaxations the solid lines represent the activation energies in terms of the slope of such lines. For the interface resistance non-linearity is obvious and the solid curve represents a guide to the eyes only.

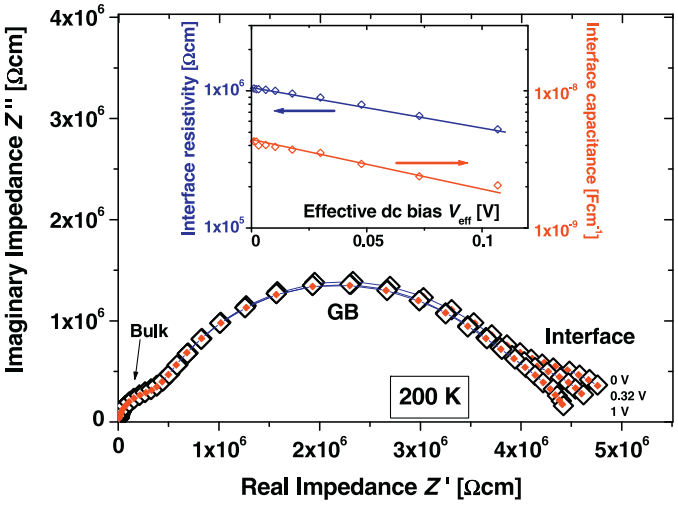


Fig. 10. Impedance spectroscopy data plotted as complex plane impedance plots of $-Z''$ vs. $Z'$ at 200 K for applied dc biases of 0, 0.32 and 1 V. Open symbols (◊) represent the data, solid squares (■) and solid lines represent fit using the equivalent circuit model shown in Fig. 9. *Inset*: Logarithmic interface resistivity and interface capacitance vs. effective dc bias $V_{\text{eff}}$.

values rather typical for the respective type of contribution.[26] It is worth noting that all 3 capacitance values show no considerable temperature dependence. This is inconsistent with previous claims that $ErCrO_3$ is ferroelectric, in which case a strong tem-perature dependence of intrinsic bulk $\varepsilon_r$ values, and general $\varepsilon_r$ values higher than the Clausius–Mossotti prediction would be expected.

The bulk, GB and interface resistivity values were plotted on Arrhenius axes as shown in Fig. 9. The bulk and GB activation energies were determined as the slopes of the Arrhenius plots to be 0.27 eV and 0.3 eV respectively. The Arrhenius curve for the interface resistance is bended but can be linearised by using variable-range-hopping (VRH) axes with a hopping exponent of $p = 0.25$ (Mott VRH hopping).[31]

### 3.4. *Schottky type Au/$ErCrO_3$ interface barrier*

Furthermore, at a f xed temperature of 200 K a variable underlying dc bias was applied to the impedance test signal in order to measure the dc bias dependence of all equivalent circuit parameters. The data in Fig. 10 shows a clear dependence on dc bias of the interface relaxation (R3-CPE3) at all temperatures, which is consistent with the interpretation of a Au electrode/ceramic $ErCrO_3$ interface effect. A non-linear inter-face resistance R3 is indicated by the reduction of the size of the interface semicircle in plots of $-Z''$ vs. $Z'$. It has to be noted that the interface resistance is smaller here as com-pared to Fig. 7, possibly because the sample had been heated to 550 K beforehand during the temperature dependent measurements. This heat exposure probably constituted an annealing effect of the electrode/sample interface resulting in a reduced interface resistance for the consecutive measurement of the dc bias dependence at 200 K. Alternatively, the applied ac or dc bias or the resulting currents may have caused alterations to the interface structure. The bulk and GB resistances show very similar values in Figs. 7 and 9; small differences may be due to a small temperature lag, since the temperature dependent IS data was measured upon heating and the dc bias depen-dence was measured after cooling back to 200 K. The data for different applied dc biases was fitte to the model shown in Fig. 7, resulting in excellent fits and the dc bias dependence of the interface resistance (R3) and interface capacitance (CPE3) were obtained. The inset of Fig. 10 shows the interface resistivity (R3) and corrected capacitance (C3) vs. the effective dc bias $V_{\text{eff}}$, which was calculated as the actual voltage that drops across one Au/$ErCrO_3$ interface. The interface resistance R3 and capacitance showed both clear exponential non-linearity as demonstrated in the logarithmic plots in the inset of Fig. 10, which is the typical Schottky behavior at interfaces of metal electrodes and semiconducting oxides.[32] It was attempted to calculate the potential barrier height or built in potential $\Phi_B$ of the Schottky barrier interface from plots of $(1/C3 - 1/2C3_0)^2$ vs. $V_{\text{eff}}$,[33,34] where $C3_0$ is the interface capacitance at zero applied dc bias. However, such plots yielded unphysically low $\Phi_B$ val-ues of $\Phi_B$ = 30.5 mV and generally poor linearity at higher dc bias values. This rather irregular barrier behavior and the drastic changes of the interface resistance with temperature and/or applied voltage/current response (see Figs. 7 and 10) may imply that hysteretic ferroelectric polarization measurements may be problematic in this material. If a perceptible part of the ferroelectric test signal voltage applied to the sample drops in a rather unconventional fashion at an electrode–sample interface, the results from previous ferroelectric hysteresis loop measurements claiming ferroelectricity should be considered with care. The remaining two bulk and GB relaxations R2-CPE2 and R1-CPE1 did not exhibit any perceptible dc bias dependence as shown by the approximately constant size of the semicircles in $-Z''$ vs. $Z'$ (Fig. 10).

## 4. Conclusions

We have shown that the microwave assisted synthesis process is adequate to produce single-phase orthorhombic, tilted perovskite $ErCrO_3$ samples. Rietveld refinemen analysis of XRD data suggested that $ErCrO_3$ crystallizes in the centro-symmetric space group Pnma, which is consistent with the rather low dielectric permittivity in the range of a standard dielectric material ($\varepsilon_r \approx 23$) without any perceptible temperature dependence. The typical signs of ferroelectricity were all missing. The compound was found to be predominantly anti-ferromagnetic with a small ferri-magnetic moment ($\approx 0.4\,\mu_B$) and a Neel transition temperature of $T_{Neel} \approx 135$ K. The Au electrode/$ErCrO_3$ ceramic interface showed the signs of a rather unconventional type of Schottky barrier.

## Acknowledgments

J.P.-G. acknowledges financia help from the Community of Madrid (Materyener S2009/PPQ-1626) and a PhD scholarship from the Universidad Complutense de Madrid. R.S. wishes to acknowledge the Ministerio de Ciencia e Innovacion (MICINN) for granting a "Ramón y Cajal" Fellowship. Furthermore, this work was supported by the MICINN through grant no. MAT 2007-31034 and MAT2010-19460. The authors wish to express their gratitude to Dr. Julio Romero de Paz for technical assistance with the magnetic measurements, and to Prof. Jacobo Santamaria, Prof. Carlos León and Dr. Oscar Juan Durá for allowing use of and for assistance with the impedance spectroscopy facilities.

## References

1. Sahu JR, Serrao CR, Ray N, Waghmare UV, Rao CNR. Rare earth chromites: a new family of multiferroics. *J Mater Chem* 2007;**17**: 42.
2. Sardar K, Lees MR, Kashtiban RJ, Sloan J, Walton RI. Direct hydrothermal synthesis and physical properties of rare-earth and yttrium orthochromite perovskites. *Chem Mater* 2011;**23**:48.
3. Su Y, Zhang J, Li L, Li B, Zhou Y, Deng D, Chen Z, Cao S. Temperature dependence of magnetic properties and change of specifi heat in perovskite $ErCrO_3$ chromites. *Appl Phys A* 2010;**100**:73.
4. Fuentes-Cobas LE, Matutes-Aquino JA, Fuentes-Montero ME. In: Buschow KHJ, editor. *Handbook of magnetic materials*, vol. 16. Amsterdam, Netherlands: Elsevier; 2011 [Chapter 3].
5. Durán A, Arévalo-López AM, Castillo-Martínez E, García-Guaderrama M, Morán E, Cruz MP, Fernández F, Alario-Franco MA. Magneto-thermal and dielectric properties of biferroic $YCrO_3$ prepared by combustion synthesis. *J Solid State Chem* 2010;**183**:1863.
6. Mitchell RH. *Perovskites modern and ancient*. Canada: Almaz Press Inc.; 2002. p. 20.
7. Ramesha K, Llobet A, Proffen T, Serrao CR, Rao CNR. Observation of local non-centrosymmetry in weakly biferroic $YCrO_3$. *J Phys: Condens Matter* 2007;**19**:102202.
8. Satoh H, Koseki S-I, Takari M, Chung WY, Kamegashira N. Heat capacities of $LnCrO_3$ (Ln = rare earth). *J Alloys Compd* 1997;**259**:176.
9. Kuznetsov MV, Parkin IP. Convenient, rapid synthesis of rare earth orthochromites $LnCrO_3$ by self-propagating high-temperature synthesis. *Polyhedron* 1998;**17**:4443.
10. Parkin IP, Komarov AV. Alternative solid state routes to mixed metal oxides $LnCrO_3$, $LnFeO_3$. *Polyhedron* 1996;**15**:3117.
11. Prado-Gonjal J, Arévalo-López ÁM, Morán E. Microwave-assisted synthesis: a fast and efficien route to produce $LaMO_3$ (M = Al, Cr, Mn, Fe, Co) perovskite materials. *Mat Res Bull* 2011;**46**:222.
12. Iwasaki M, Takizawa H, Uheda K, Endo T, Shimada M. Microwave synthesis of $LaCrO_3$. *J Mater Chem* 1998;**8**:2765.
13. Hayes BL. *Microwave synthesis*. Matthews: CEM Publishing; 2002. p. 19.
14. Zhao J, Yan W. In: Xu R, Pang W, Huo Q, editors. *Modern inorganic synthetic chemistry*. Amsterdam, Netherlands: Elsevier; 2010 [Chapter 8].
15. Gupta M, Leong EWW. *Microwaves and metals*. Singapore: John Wiley & Sons (Asia); 2007. p. 35.
16. Rao KJ, Vaidhyanathan B, Ganguli M, Ramakrishnan PA. Synthesis of inorganic solids using microwaves. *Chem Mater* 1999;**11**:882.
17. Prado-Gonjal J, Villafuerte-Castrejón ME, Fuentes L, Morán E. Microwave–hydrothermal synthesis of the multiferroic $BiFeO_3$. *Mat Res Bull* 2009;**44**:1734.
18. Morniroli JP, Steeds JW. Microdiffraction as a tool for crystal structure identificatio and determination. *Ultramicroscopy* 1992;**45**:219.
19. Digital Micrograph software 1.71.38 Gatan, Inc.
20. MacTempas Software (Version 2.3.7, Roar Kilaas).
21. Jiménez E, Isasi J, Fernández MT, Sáez-Puche R. Magnetic behavior of $ErCrO_4$ oxide. *J Alloys Compd* 2002;**344**:369.
22. Gjonnes J, Moodie AF. Extinction conditions in the dynamic theory of electron diffraction. *Acta Crystallogr* 1965;**19**:65.
23. Williams DB, Carter CB. *Transmission electron microscopy: a textbook for materials science*. New York: Springer; 2009.
24. Morishita T, Tsushima K. Susceptibility of the weak ferromagnets $ErCrO_3$ and $YCrO_3$ near the critical anomaly. *Phys Rev B* 1981;**24**:341.
25. Sharim N, Shaked H, Schtrikman S. Magnetic structure of some rare-earth orthochromites. *Phys Rev B* 1981;**24**:6642.
26. Irvine JTS, Sinclair DC, West AR. Electroceramics: characterization by impedance spectroscopy. *Adv Mater* 1990;**2**:132.
27. Barsukov E, Macdonald JR. *Impedance spectroscopy: theory, experiment and applications*. Hoboken, USA: John Wiley & Sons Inc.; 2005.
28. Díez A, Schmidt R, Sagua AE, Frechero MA, Matesanz E, Leon C, Morán E. Structure and physical properties of nickel manganite $NiMn_2O_4$ obtained from nickel permanganate precursor. *J Eur Ceram Soc* 2010;**30**: 2617.
29. Hsu CH, Mansfeld F. Concerning the conversion of the constant phase element parameter $Y_0$ into a capacitance. *Corrosion* 2001;**57**: 747.
30. Shannon RD. Dielectric polarizabilities of ions in oxides and fluorides *J Appl Phys* 1993;**73**:348.
31. Schmidt R, Basu A, Brinkman AW. Small polaron hopping in spinel manganates. *Phys Rev B* 2005;**72**:115101.
32. McKelvey JP. *Solid state and semiconductor physics*. New York, USA: Harper & Row; 1966.
33. Mukae K, Tsuda K, Nagasawa I. Capacitance vs voltage characteristics of ZnO varistors. *J Appl Phys* 1979;**50**:4475.
34. Adams TB, Sinclair DC, West AR. Characterization of grain boundary impedances in fine and coarse-grained $CaCu_3Ti_4O_{12}$ ceramics. *Phys Rev B* 2006;**73**:094124.